

Submitted to *Astronomical Journal*

**ACCURATE DETERMINATION OF THE MASS DISTRIBUTION IN
SPIRAL GALAXIES:
II. Testing the Shape of Dark Halos**

SÉBASTIEN BLAIS–OUELLETTE¹

*Département de physique and Observatoire du mont Mégantic, Université de Montréal, C.P.
6128, Succ. centre ville, Montréal, Québec, Canada. H3C 3J7 and
Observatoire de Marseille, 2 Place Le Verrier, F-13248 Marseille Cedex 04, France
e-mail: blaisous@lml.gov*

PHILIPPE AMRAM

*bservatoire de Marseille, 2 Place Le Verrier, F-13248 Marseille Cedex 04, France
e-mail: amram@observatoire.cnrs-mrs.fr*

CLAUDE CARIGNAN²

*Département de physique and Observatoire du mont Mégantic, Université de Montréal, C.P.
6128, Succ. centre ville, Montréal, Québec, Canada. H3C 3J7
e-mail: carignan@astro.umontreal.ca*

ABSTRACT

New high resolution CFHT Fabry–Perot data, combined with published VLA 21 cm observations are used to determine the mass distribution of NGC 3109 and IC 2574. The multi-wavelength rotation curves allow to test with confidence different dark halo functional forms from the pseudo-isothermal sphere to some popular halo distributions motivated by N-body simulations. It appears that density distribution with an inner logarithmic slope ≤ -1 are very hard to reconcile with rotation curves of late type spirals. Modified Newtonian Dynamics (MOND) is also considered as a potential solution to missing mass and tested the same way. The new higher resolution data show that MOND can reproduce in details the rotation curve of IC 2574 but confirm its difficulty to fit the kinematics of NGC 3109.

^aActual address: Inst. of Geophysics & Planetary Physics, Lawrence Livermore National Lab., CA 94550, USA

^bVisiting Astronomers, Canada–France–Hawaii Telescope, operated by the National Research Council of Canada, the Centre National de la Recherche Scientifique de France, and the University of Hawaii.

Subject headings: cosmology: dark matter — galaxies: individual (NGC 3109, IC 2574, NGC 5585, NGC 3198)
— galaxies: fundamental parameters (masses) — techniques: interferometric

1. Introduction

Over the last 30 years, rotation curves have been a very efficient tool to study the mass distribution in spiral galaxies. They clearly brought to light the important discrepancy between the luminous mass and the gravitational mass that has led to the supposition of a large amount of dark matter in the Universe. The now commonly accepted picture is that this unseen matter takes the form of large halos in the center of which galaxies are embedded. Alternatively, the gravitational attraction could deviate from the pure Newtonian force at very low acceleration so that no dark matter is necessary.

The resolution reached by N-body simulations of the cosmic evolution of dark halos (Navarro et al. 1996b, 1997; Fukushige & Makino 1997; More et al. 1998; Kravtsov et al. 1998) allows one to predict the inner part of halo density profiles. In theory, these profiles could be directly compared to the ones deduced from modeling the rotation curves. Unfortunately, the sensitivity of the rotation curves to the exact density profile of the halos is quite low and one must use the highest sensitivity and the highest resolution possible to arrive at useful comparisons (Blais-Ouellette et al. 1999, hereafter paper I).

This study investigates primarily, in the context of Newtonian gravitation, the density profile of the dark halos of two late type spiral galaxies: NGC 3109 and IC 2574. As late type, their bulge is minimal making them well suited objects for sensitive mass distribution studies because of the reduced uncertainties due to the negligible spheroid contribution in the inner parts. Mass models of NGC 3109 based on radio observations have already been presented by Jobin & Carignan (1990) while the dark matter distribution in IC 2574 have been studied by Martimbeau et al. (1994). New high resolution Fabry-Perot observations of the H α emission line are used in combination with the published 21 cm data to form accurate multi-wavelength rotation curves. These curves are used to model the mass distribution in the galaxies. The models include a stellar disk, a gaseous component and a dark spherical halo.

Moreover, NGC 3109 has often been presented as a test for the Modified Newtonian Dynamics (Milgrom 1983). As noted in Broeils (1992), the inner part of the rotation curve is crucial to draw any conclusion on the MOND fit to this galaxy. Therefore, the mass models of the two galaxies based on the MOND assumption are presented as well.

The CFHT Fabry-Perot observations are described in Section 2 while the mass models of the two galaxies, to which we add NGC 5585 and NGC 3198 from paper I, are discussed in Section 3

2. New Fabry–Perot Observations

The Fabry-Perot observations of the H α emission line were obtained in February 1994 at the Canada–France–Hawaii Telescope (CFHT). The etalon (CFHT1) was installed in the CFHT’s Multi–Object Spectrograph (MOS). A narrow–band filter ($\Delta\lambda \approx 12 \text{ \AA}$), centered at $\lambda_0 = 6565.5 \text{ \AA}$ for NGC 3109 ($V_{sys} \approx 402 \text{ km s}^{-1}$) and at $\lambda_0 = 6559.5 \text{ \AA}$ for IC 2574 ($V_{sys} \approx 53 \text{ km s}^{-1}$), was placed in front of the etalon. The available field with no vignetting was $\approx 8.5' \times 8.5'$, with $0.314'' \text{ px}^{-1}$. The free spectral range of 5.66 \AA (259.5 km s^{-1}) was scanned in 27 (+1 overlapping) channels, giving a sampling of 0.21 \AA (9.6 km s^{-1}) per channel. Eight minutes integration were spent at each channel position. Table 1 lists the complete observing parameters.

Following normal de–biasing and flat–fielding with standard IRAF procedures, a robust 3-D cosmic–ray removal routine, that tracks cosmic rays by spatial (pixel–to–pixel) and spectral (frame–to–frame) analysis, was applied. Ghost reflections were then removed using the technique described in Paper I.

With the ADHOC software package^c, photometric variations were corrected using the mean night sky (background + emission lines) to calculate the corrections to apply to each frame.

Then, a calibration based on a neon lamp ($\lambda 6598.95 \text{ \AA}$) was used to fix the zero point of the spectrum at each pixel.

2.1. NGC 3109

Table 2 gives the optical parameters of NGC 3109. In order to get sufficient signal–to–noise throughout the velocity fields, two different Gaussian spatial smoothings ($\sigma=3.5$ and 5 pixels) were performed on the cube (all the channels). Velocity maps were then obtained from the intensity weighted means of the H α peaks to determine the radial velocity for each pixel. Final variable resolution velocity map (Fig. 1, top) was built keeping higher resolution for regions with originally higher signal-to-noise. The full resolution H α image is also shown on the lower part of Fig. 1.

The rotation curve was obtained from the velocity field using two different methods. The first estimate was made using the task ROCUR (Begeman 1987; Côté et al. 1991) in the AIPS package, where tilted annuli in the plane of the galaxy (ellipses in the plane of sky) are fitted to the velocity field, minimizing the dispersion inside each ring. The dynamical center, systemic velocity, position angle and inclination were estimated this way. Secondly, the ADHOC package was used to fine–tune these parameters by comparison of both sides of the galaxy and examination of the residual velocity field (see Amram et al. 1992, for the detailed method). Systemic velocity was found to be 402 km s^{-1} , very close to the value of 404 km s^{-1} found with the HI observations of Jobin & Carignan (1990). Since a warp is clearly present even in the optical velocity field, the final

^c<http://www-obs.cnrs-mrs.fr>

rotation curve was derived with ROCUR leaving the inclination and the position angle free to vary. In this context, the slightly high value of the first velocity point can be understood by the poor determination of the inclination in the center of the galaxy. Table 6 gives the full rotation curve at 20'' resolution while Fig. 2 illustrates the rotation curve as well as the variation of inclination and position angle. Following Jobin & Carignan (1990), the rotation curve was corrected for asymmetric drift.

To the present date, no convention on the way to represent the errors on rotation curves exists in the literature. Error bars are often simply given as the velocity dispersion in the ring used at each radius. However, the hot gas is known to be more sensitive to its environment than the cold gas. Turbulence, local density variations (like spiral arms, bars, etc.) and winds from stars and supernovae of the young stellar forming regions in which the ionized gas is found, increase its dispersion. This can lead to the paradox where the fewer points you have (as in long slit observations) the lower is your dispersion and the smaller are your error bars. As a more direct probe of the uncertainties on the measured potential, the difference between the two sides of the galaxy is instead often used. Some authors will add the error due to uncertainties on inclination and/or position angles.

To clearly differentiate the source of errors, the error bars shown here indicate the error on the mean in each ring (σ/\sqrt{N}) while the solutions for each side of the galaxy are represented by lines (continuous for the receding side and dashed for the approaching). Their difference is a good estimate of the asymmetry and large scale non-circular motions.

The velocity field of NGC 3109 shows many bubble-like features probably due to intense star formation especially close to the center of the galaxy. The effect of H α bubbles are normally of two kinds: first, if the front and back sides of a bubble are equally intense and the medium transparent, a broadened or even, depending of the resolution, a doubled H α line could be seen. The true gravitational rotation can still be deduced by averaging the two peaks. However, in many cases only the front side of an expanding bubble can be seen, making it difficult to retrieve the true rotational velocities.

In the case of NGC 3109, analysis of the velocity field shows a small deviation from circular motion in the inner part of the galaxy. The velocity of the single innermost point of the rotation curve is slightly affected.

Despite some internal peculiar velocities, apparently well averaged out, a relatively good agreement can be seen between the two sets of data. The HI velocities (where no beam-smearing correction have been applied) were just slightly underestimated in the inner part. This is not really surprising considering that beam smearing effects should diminish as the slope of the inner rotation curve lowers for a given beam width. The multi-wavelength rotation curve is thus composed of the H α data points up to 410'' and of HI velocities for the rest.

2.2. IC 2574

A similar reduction procedure was applied to IC 2574 and the velocity field is shown juxtaposed to the monochromatic image in Fig. 3. The first evidence is that IC 2574 is more disrupted than NGC 3109. With such a patchy velocity field, a determination of a reliable rotation curve with an iterative method based on velocity dispersion in annuli turned out to be impossible. Direct calculation of the rotation velocity for each pixel was thus done using fixed values for the position angle and the inclination. The dynamical parameters were found by comparing the two sides of the galaxy and by analyzing the residual field. The obtained rotation curve is presented in Table 7 based on a systemic velocity of 53 km s^{-1} , a position angle of 52° and an inclination of 75° , almost identical to the parameters found by Martimbeau et al. (1994) from the HI observations.

The $\text{H}\alpha$ rotation curve follows more or less the same kind of perturbations as those seen in the HI curve. For example, when one compares the two sides of the HI curve in the Fig. 8 of Martimbeau et al. (1994): (i) the effect of a giant bubble can clearly be seen at both wavelengths around $240''$ on the approaching side; (ii) the giant north–eastern OB association clearly shows up between $7'$ and $10'$ of the receding side; (iii) on another hand, some probable non-circular motions are seen around $100''$ in the $\text{H}\alpha$ but does not show up in the HI .

Since the $\text{H}\alpha$ data show no sign of beam smearing effect, there would be no reason here to use the disrupted $\text{H}\alpha$ curve instead of the 21 cm data as probe of the gravitational potential of the galaxy.

3. Mass Models and Parameters of the Mass Distribution

3.1. Comparison of different models using standard gravity

The method used in this paper to model the mass distribution is a slight generalization of the one described in Carignan & Freeman (1985).

The luminosity profile, if possible in the near infrared to probe the mass dominant stellar component, is transformed into a mass distribution for the stellar disk, assuming a constant mass–to–light ratio ($(\mathcal{M}/L_B)_*$) (Casertano 1983; Carignan & Freeman 1985). For the contribution of the gaseous component, the HI radial profile scaled by 1.33 is used to account for He. The difference between the observed rotation curve and the computed contribution to the curve of the luminous (stars & gas) component is thus the contribution of the dark component which can be represented by a dark spherical halo.

Many studies approximate later type spirals such as NGC 3109 and IC 2574 as being totally made of dark matter, neglecting the stellar and gaseous components. This is a good approximation down to a certain radius. However, the innermost parts of the rotation curves are crucial to test the shape of the density profiles. Best fit models that include the contributions of gas and stars

are therefore used to avoid an overestimation of the dark halo contribution.

Following Kravtsov et al. (1998, hereafter KKBP) and Zhao (1996), we use an even broader family of density profiles for the halo:

$$\rho(r) = \frac{\rho_0}{(c + (r/r_0)^\gamma) (1 + (r/r_0)^\alpha)^{(\beta-\gamma)/\alpha}} \quad (1)$$

where ρ_0 and r_0 are characteristic density and radius, $c=1$ forces the presence of a flat density core and α , β and γ are shape parameters.

One can either fit the value of $(c, \alpha, \beta, \gamma)$ to a particular density profile or set them to a desired value: $(1, \alpha \neq 0, 2, 2)$ for a pseudo-isothermal sphere (Begeman 1987); $(0, 1, 3, 1)$ for a NFW type halo (Navarro et al. 1996b); $(1, 2, 3, 1)$ for halos with flat density cores proposed by Burkert (1995) or $(0, 2, 3, 0.2)$ as proposed by KKBP. These four density profiles are presented in Fig. 5. Profiles with non-constant density cores ($\lim_{r \rightarrow 0}(\rho) \neq \rho_0$), are defined as cuspy. For these profile, the inner slope is given by $-\gamma$, the outer slope by β while α controls the turnover point.

NGC 3109 is particularly well suited for dynamical studies: First because its luminous component is minimal (B-band photometry from Kent 1987) so that the uncertainties related to the unknown mass-to-light ratio of the disk do not have a significant impact. Second, this galaxy is close enough to allow direct distance estimation via multicolor observation of a large number of Cepheids (Musella et al. 1997). The adopted distance is 1.36 Mpc.

In Fig. 6 and 7, best-fit models are given for the rotation curves of NGC 3109 and IC 2574 respectively. The high resolution data (used up to 410 " for NGC 3109) remove some uncertainties pointed out by Navarro (1997) on the difference in HI curves coming from different generation of radio-telescopes (single dish and aperture synthesis). It confirms the great difficulty to reconcile the cuspy profile with $\gamma \geq 1$ and the rotation curve of a late type spiral like NGC 3109. Either constant density core profiles or mildly cuspy profiles with $\gamma \ll 1$ can fit the data adequately. It is very difficult to discriminate between a density distribution with a flat core from one with a mild cusp because r_0 can often be stretched to a point where the two types of profile match. One has to go to very small radii ($\lesssim \gamma r_0$) to really probe any incompatibility.

Cuspy profiles with $\gamma \geq 1$ seem naturally obtained from CDM N-body simulations but many models have been suggested that deviate somewhat from the standard CDM assumptions and avoid the creation of a steep central density cusp. As noted by KKBP, Syer & White (1998) showed that γ is sensitive to the past merger rate and to the perturbation power spectrum on the scale of a galactic halo. Therefore a less active merger history or a steeper power spectrum should lead to $\gamma < 1$ on galactic scale. Self-interacting dark matter (Spergel & Steinhardt 1999) has also been suggested to suppress the formation of high density dark matter cusp but the implied inverse dependency of the core radius on the mass of the galaxy (Dalcanton & Hogan 2000) is not observed in our sample.

Alternatively, in order to explain the presence of flat density core in dwarf spirals for standard,

scale free CDM models, Navarro et al. (1996a) suggested that violent starburst could eject the gas and consequently flatten the inner dark matter distribution. Semi-analytical calculations gives this scenario the right order of magnitude for a low mass galaxy given a sufficient feedback efficiency (van den Bosch et al. 2000).

Another way to reconcile the too steep rotation curves without invoking a flat density CDM core is to add a second, compact object component to the non-baryonic cold dark matter (Burkert & Silk 1997). Of course this adds some degrees of freedom when fitting rotation curves and a better fit is in this case somewhat meaningless, making this hypothesis hard to test. A better knowledge of the importance and distribution of Massive Compact Halo Objects (MACHOs) in our own Galaxy would address the relevance of this hypothesis.

NGC 5585 is also well fitted by all the profiles but the NFW (8). The slight difference between the $(\mathcal{M}/L_B)_*$ found here (0.85) and the one found in paper I (0.80) is due to the use of the equation 1 instead of the integration of the Poisson’s equation of the isothermal sphere.

In the case of NGC 3198 (Fig. 9), all the profiles are compatible. The $H\alpha$ curve has been used up to 65 " to rectify the overcorrection of the beam smearing in Begeman (1987). The only remark to be made is that all the profile are too smooth to account for the small variations in the outer rotation curve, even though they are present in both the HI and the B profile. The detailed gravitational interplay between luminous and dark matter should be taken into account.

3.2. Modified Newtonian Dynamics

Proposed by Milgrom (1983), a modification of Newtonian gravitation in the low acceleration limit can mimic a large amount of dark matter in spiral galaxies. MOND is a truly falsifiable theory: it contains only one parameter, a_0 , that is supposed to be a universal constraint. A lot of work have been done using rotation curves where the quality of the data gives the best opportunity to test the theory (e.g. Begeman et al. 1991; Sanders 1996; Sanders & Verheijen 1998; McGaugh & De Blok 1998).

As a reminder, here is the MOND quantitative prescription. For purely circular motion, one can equate the centripetal acceleration and gravitational acceleration. In the Newtonian regime, we simply get the common

$$\frac{V^2}{R} = \frac{GM_T}{R^2} = g_N \quad (2)$$

The MODified Newtonian Dynamics (MOND) state that the true acceleration is given by

$$\mu(g/a_0)\mathbf{g} = \mathbf{g}_N \quad (3)$$

where $\mu(g/a_0)$ is an interpolation function that has the right asymptotic behavior: $\mu(g/a_0 \gg 1) \rightarrow 1$ and $\mu(g/a_0 \ll 1) \rightarrow g/a_0$.

The exact form of $\mu(g/a_0)$ has no impact on the mass models of very late type spirals like NGC 3109 and IC 2574 where the gravitational acceleration is well below a_0 at all radii but in general, the commonly used

$$\mu(x) = \frac{x}{\sqrt{1+x^2}} \quad (4)$$

is assumed to be the interpolation function.

In the limit of low acceleration the gravitational acceleration is thus given by $g = \sqrt{a_0 g_N}$ and

$$\frac{V^2}{R} = \sqrt{\frac{GM_T}{R^2} a_0} \quad (5)$$

or

$$V^4 = GM_T a_0 \quad (6)$$

which naturally explains the asymptotic flatness of rotation curves and the Tully-Fisher relation.

A best-fit method, similar to the one used for dark halos has been applied. The stellar luminosity profile and the HI density profile are this time transformed into a mass distribution following equations (3) and (4). The free parameter of the fit is as always the $(M/L)_*$ ratio. a_0 is considered as a universal constant but since no fundamental theory exists as of yet to give its true value, four different values are used in the fits. First, the value found by Begeman et al. (1991) that best fits their highly selective and high quality sample (1.2×10^{-13} km/s). The second value is the one that best fits each present galaxy individually (Table 5). The two other values are educated guesses of what could be a_0 in an underlying theory, as suggested by Milgrom (1998). For instance, $cH_0 = 6.8 \times 10^{-13}$ km/s² where c is the speed of light and $H_0 = 71 \pm 6$ km s⁻¹ (Mould et al. 2000) and $c^2 \sqrt{\Lambda} = 7.8 \times 10^{-13}$ km/s² where $\Lambda \simeq 2.3 \times 10^{-51}$ cm⁻² if $\Omega_M = 0.3$ as indicated by the recent data on high redshift supernovae (Perlmutter et al. 1999). Fig. 10 shows the best fit for each galaxy and Table 5 indicates the parameters when using the best fitted a_0 .

IC 2574 and NGC 3198 are fairly well fitted by the MOND law if the “universal constant” a_0 is let free to vary by more than a factor 2. The quality of the fit is especially good in the case of IC 2574 where most of the features of the rotation curve are reproduced in the fit. On the other side, the MOND prescription has more difficulties to account for the mass distribution of NGC 3109 and NGC 5585 whatever the value of a_0 . Being for large part in the Newtonian regime, the case of NGC 5585 is somewhat less significant as it probes more the interpolation function than the MOND theory itself. At the opposite, NGC 3109 belongs fully to the MOND regime. Even though the H α velocities are somewhat higher than the HI near the center, the rise of the rotation curve is still too shallow to be compatible with MOND. The uncertainties on NGC 3109 rotation curve have been seriously narrowed and the improved rotation curve still put the MOND theory in difficulty.

4. Summary and Discussion

With the four galaxies studied so far, it is clear that while there is a good agreement between Fabry-Perot and HI data for the shallow rotation curves of the late type galaxies NGC 3109 and IC 2574, the beam smearing plays an important role for the steeper rotation curves. The beam smearing thus seems to depend on at least two factors: the inner slope of the rotation curve and the sampling of the curve, often expressed as the ratio of the Holmberg radius to the beam width (Bosma 1978). Bosma suggested a ratio greater than 6 to have reliable HI curve. This ratio is about 9 for NGC 5585 and 30 for NGC 3109 and the later is still slightly affected by beam smearing.

Using the multi-wavelength rotation curves to determine the density profiles of dark matter halos, it appears clearly that cuspy profiles with inner logarithmic slope $\gamma \geq 1$ do not match the observations. The best fits are achieved using either a slightly cuspy profile with a very shallow inner slope or a profile with a flat density core. If most of the simulations describe a realistic CDM evolution, an additional process is needed to destroy or forbid the formation of a central cusp. However, none of the actually proposed scenarios stand out as the most plausible either because they are not easily testable or their predictions do not appear clearly in the data.

The Modified Newtonian Dynamics prescription can fit the rotation curves of IC 2574 and NGC 3198 obtained from the new high resolution data if a_0 is free to vary by a factor of 2. In this case, most of the features of the rotation curve are even reproduced with the right amplitude. Of course, since there is almost no stellar disk, at least in the part fully in the MOND regime, scaling the HI would produce a similar result. Can H_2 be involved here? (Pfenniger et al. 1994). On the other hand, the variations of the stellar and gaseous components also possibly just follow a non-smooth dark matter distribution.

Things are quite different in the case of NGC 3109. The slight increase of the inner velocities brought by the H α data is not sufficient to significantly improve the compatibility between the MOND theory and this galaxy even if the uncertainties have been seriously narrowed. It has to be noted though, that the amplitude of the features in the curve are also well reproduced here.

There is always a danger to let what should be a universal constant like a_0 vary to fit the data. However, since no underlying theory exists yet, it is interesting to note that for these late type spirals, a_0 seems systematically higher than for the earlier types.

5. Conclusion

The present work leads to the following conclusions:

- Observations of the kinematics of the ionized hydrogen in NGC 3109 and IC 2574 is in good agreement with the previous kinematical studies of the atomic hydrogen. This implies that the beam smearing was limited in the HI data although NGC 3109 was slightly affected.

- Overall, beam smearing can be important even for “good sampling” (20 beam widths per Holmberg radius for NGC 5585) depending on the inner slope of the rotation curve.

- The CDM models with a inner density slope $\gamma \geq 1$ are not compatible with the data on NGC 3109 and IC 2574. Flat density core models like the pseudo-isothermal sphere or a model with a shallow inner density slope are compatible with the four galaxies in our sample.

- The MOND prescription can fit the rotation curves of NGC 2574 and NGC 3198 if the “universal constant’ a_0 is free to vary by more than a factor of 2. It is however unable to reproduce the mass distribution of NGC 3109 and NGC 5585 whatever the value of a_0 .

The present examples give a good idea of the impact of higher resolution rotation curves. There is however large unexplored regions in terms of galaxy mass, surface brightness and morphological types. It is thus imperative to extend this sample to earlier type galaxies covering a large range in surface brightness. This would give, among other things, the opportunity to study precisely at what point the rotation curves stop agreeing with N-body simulations.

We would like to thank the staff of the CFHT for their support during the data acquisition and Daniel Durand from DAO who helped with data acquisition. We also warmly thank Jacques Boulesteix for fruitful discussion on Fabry-Perot reduction and Piotr Popowski for valuable comments. CC acknowledges grants from NSERC (Canada) and FCAR (Québec).

REFERENCES

- Amram, P., Marcelin, M., Boulesteix, J., & Le Coarer, E. 1992, *A&A*, 266, 106
- Begeman, K. 1987, PhD thesis, Rijksuniversiteit Groningen
- Begeman, K. G., Broeils, A. H., & Sanders, R. H. 1991, *MNRAS*, 249, 523
- Blais-Ouellette, S., Carignan, C., Amram, P., & Côté, S. 1999, *AJ*, 118, 2123
- Bosma, A. 1978, PhD thesis, Rijksuniversiteit Groningen
- Broeils, A. 1992, PhD thesis, Rijksuniversiteit Groningen
- Burkert, A. 1995, *ApJ*, 447, L25
- Burkert, A. & Silk, J. 1997, *ApJ*, L55
- Carignan, C. & Freeman, K. C. 1985, *ApJ*, 294, 494
- Casertano, S. 1983, *MNRAS*, 203, 735
- Côté, S., Carignan, C., & Sancisi, R. 1991, *AJ*, 102, 904
- Dalcanton, J. J. & Hogan, C. J. 2000, *astro-ph/0004381*
- De Vaucouleurs, G., De Vaucouleurs, A., Corwin, Herold G., J., Buta, R. J., Paturel, G., & Fouque, P. 1991, *Third Reference Catalogue of Bright Galaxies (Volume 1-3, XII, 2069 pp. 7 figs.. Springer-Verlag Berlin Heidelberg New York)*
- Fukushige, T. & Makino, J. 1997, *ApJ*, 477, L9
- Jobin, M. & Carignan, C. 1990, *AJ*, 100, 648
- Kent, S. M. 1987, *A.J.*, 93, 816
- Kravtsov, A. V., Klypin, A. A., Bullock, J. S., & Primack, J. R. 1998, *ApJ*, 502, 48
- Martimbeau, N., Carignan, C., & Roy, J.-R. 1994, *AJ*, 107, 543
- McGaugh, S. S. & De Blok, W. J. G. 1998, *ApJ*, 499, 41+
- Milgrom, M. 1983, *ApJ*, 270, 365
- Milgrom, M. 1998, in *Second International Workshop on Dark Matter*, ed. H. Klapdor-Kleingrothaus & L. Baudis
- More, B., Governato, F., Quinn, T., Stadel, J., & Lake, G. 1998, *ApJ*, 499, L5

- Mould, J. R., Huchra, J. P., Freedman, W. L., Kennicutt, R. C., Ferrarese, L., Ford, H. C., Gibson, B. K., Graham, J. A., Hughes, S. M. G., Illingworth, G. D., Kelson, D. D., Macri, L. M., Madore, B. F., Sakai, S., Sebo, K. M., Silbermann, N. A., & Stetson, P. B. 2000, *ApJ*, 529, 786
- Musella, I., Piotto, G., & Capaccioli, M. 1997, *AJ*, 114, 976
- Navarro, J. F. 1997, in *ASP Conf. Ser. 117: Dark and Visible Matter in Galaxies and Cosmological Implications*, 404
- Navarro, J. F., Eke, V. R., & Frenk, C. S. 1996a, *MNRAS*, 283, L72
- Navarro, J. F., Frenk, C. S., & White, S. D. M. 1996b, *ApJ*, 462, 563
- . 1997, *ApJ*, 490, 493
- Perlmutter, S., Aldering, G., Goldhaber, G., Knop, R. A., Nugent, P., Castro, P. G., Deustua, S., Fabbro, S., Goobar, A., Groom, D. E., Hook, I. M., Kim, A. G., Kim, M. Y., Lee, J. C., Nunes, N. J., Pain, R., Pennypacker, C. R., Quimby, R., Lidman, C., Ellis, R. S., Irwin, M., McMahon, R. G., Ruiz-Lapuente, P., Walton, N., Schaefer, B., Boyle, B. J., Filippenko, A. V., Matheson, T., Fruchter, A. S., Panagia, N., Newberg, H. J. M., Couch, W. J., & Project, T. S. C. 1999, *ApJ*, 517, 565
- Pfenniger, D., Combes, F., & Martinet, L. 1994, *A&A*, 285, 79
- Sanders, R. H. 1996, *ApJ*, 473, 117
- Sanders, R. H. & Verheijen, M. A. W. 1998, *ApJ*, 503, 97
- Spergel, D. & Steinhardt, P. 1999, *astro-ph/9909386*
- Syer, D. & White, S. D. M. 1998, *MNRAS*, 293, 337
- van den Bosch, F. C., Robertson, B. E., Dalcanton, J. J., & de Blok, W. J. G. 2000, *AJ*, 119, 1579
- Zhao, H. 1996, *MNRAS*, 278, 488

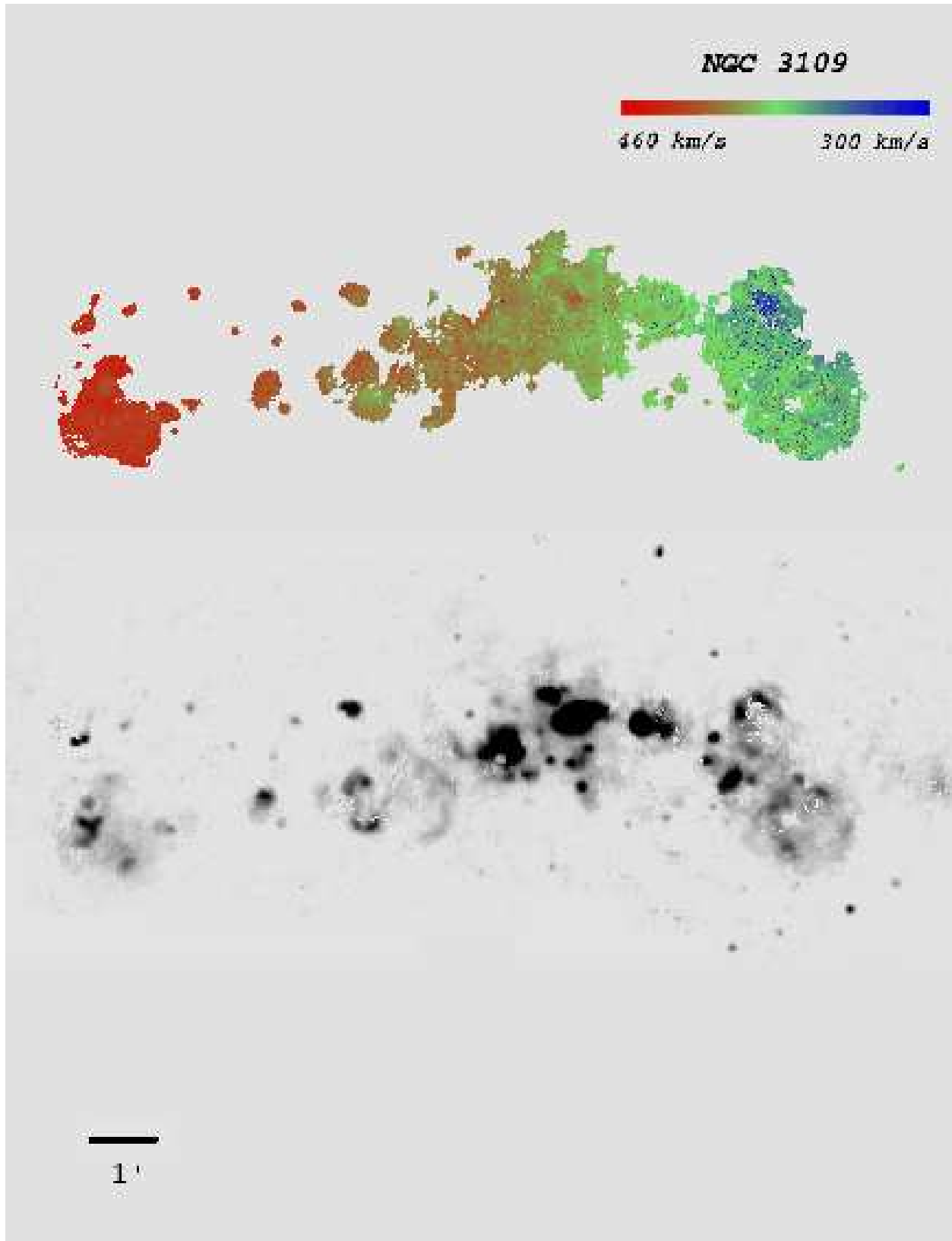


Fig. 1.— Velocity field and H α image of NGC 3109. North is up and East is left.

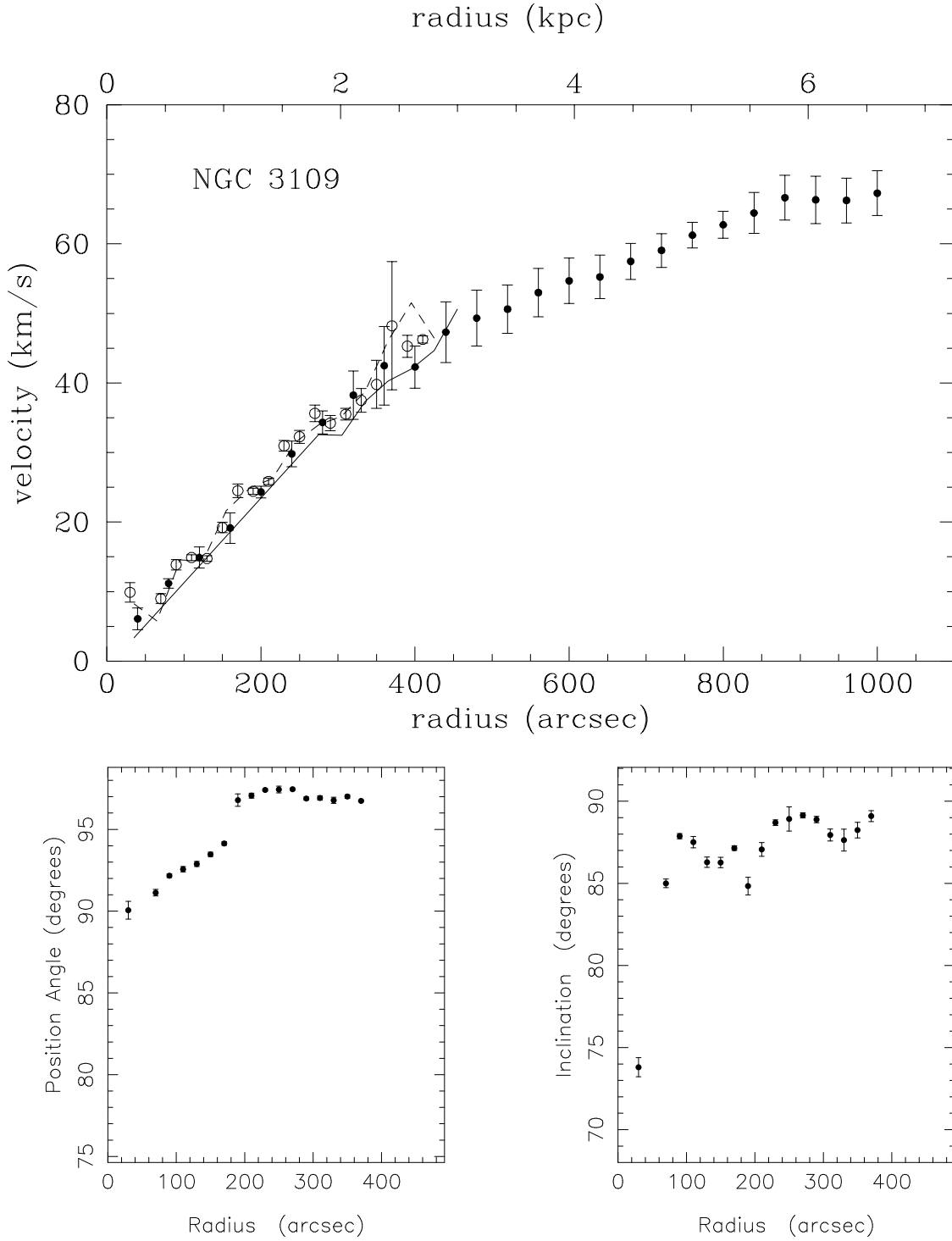


Fig. 2.— *Top* H α rotation curve of NGC 3109 (open circles) compared to the HI rotation curve (filled circles) from Jobin & Carignan (1990). The approaching and receding sides are respectively represented by the dashed and continuous lines; *bottom* variation of the position angle and inclination for the H α curve. See text for details on curves and error bars.

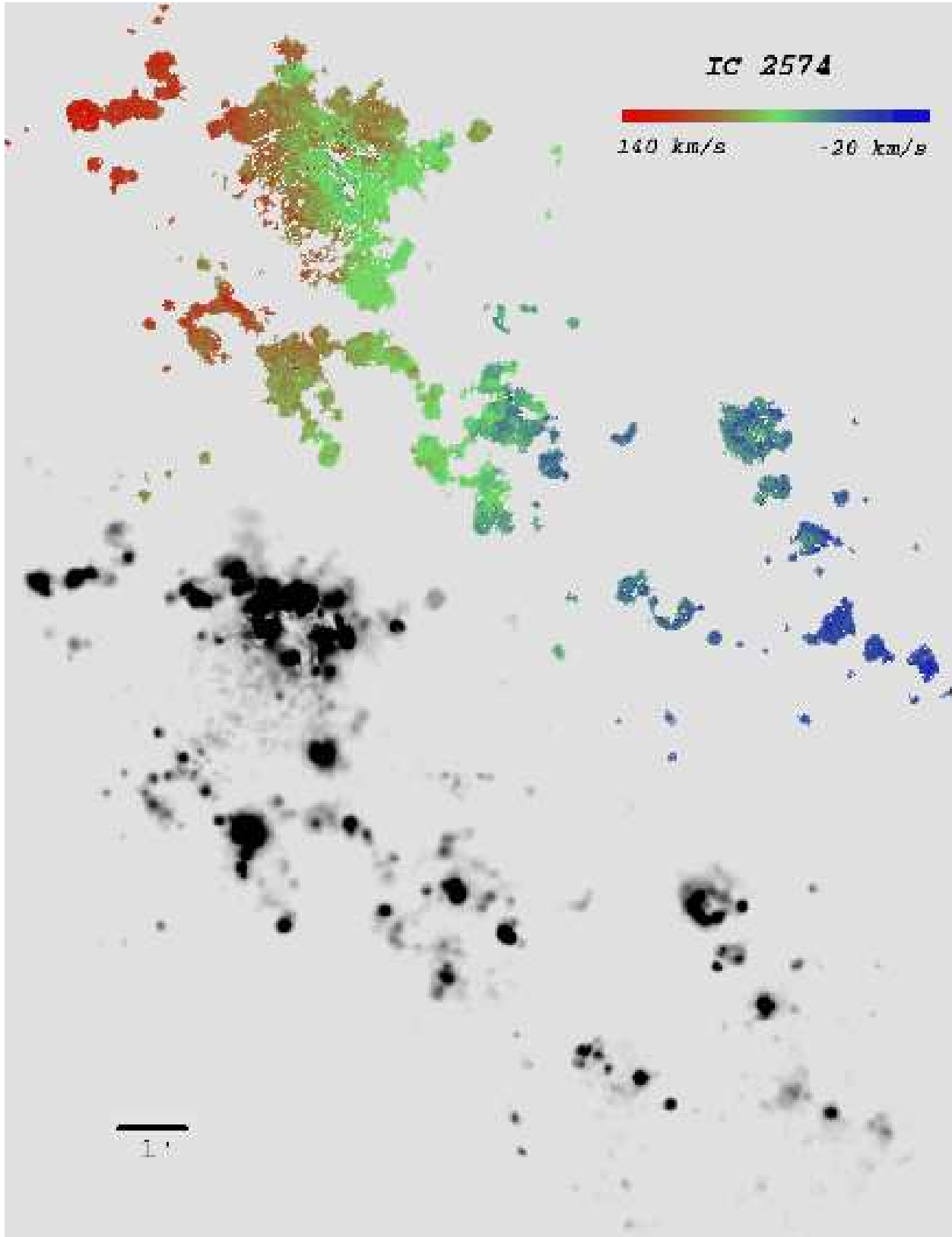


Fig. 3.— Velocity field and H α image of IC 2574. North is up and East is left.

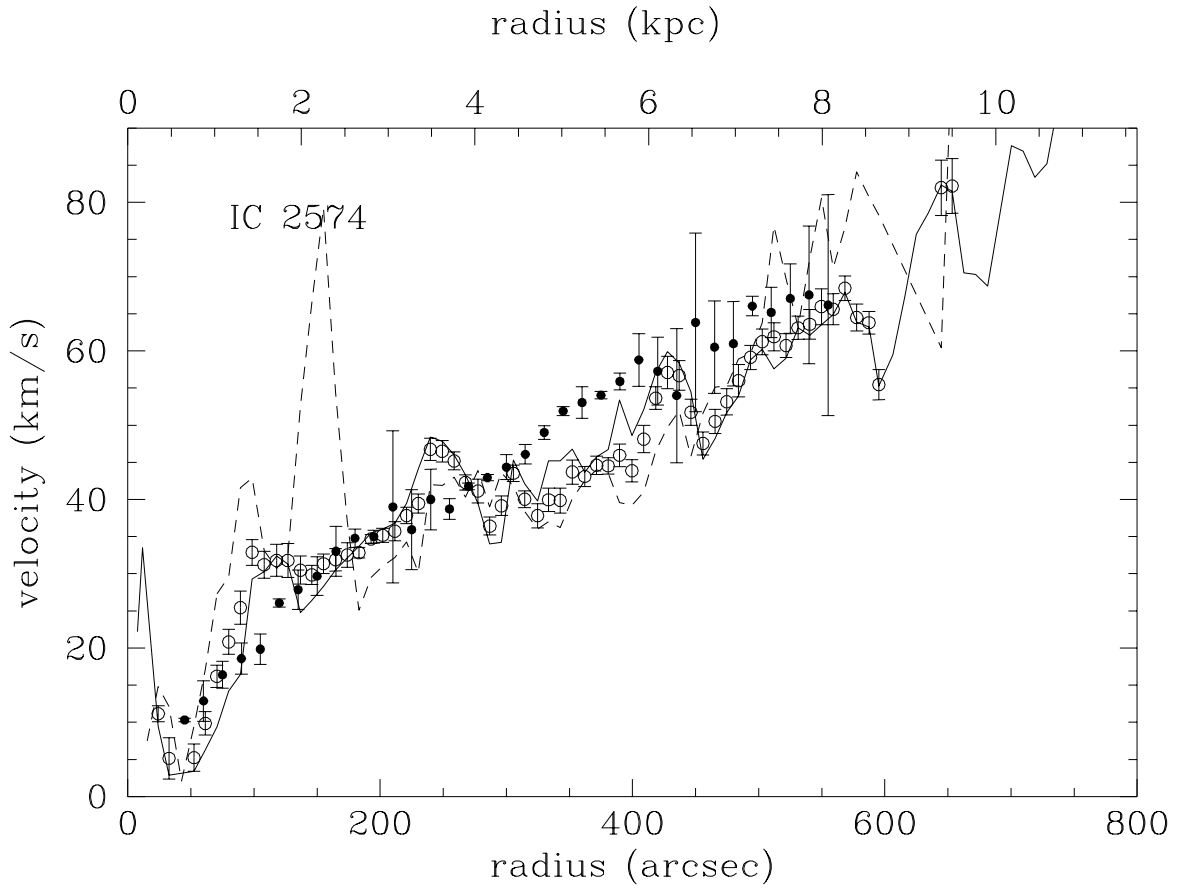


Fig. 4.— H α rotation curve of IC 2574 (open circles) compared to the HI rotation curve (filled circles) from Martimbeau et al. (1994). The approaching and receding sides of the H α curve are respectively represented by the dashed and continuous lines.

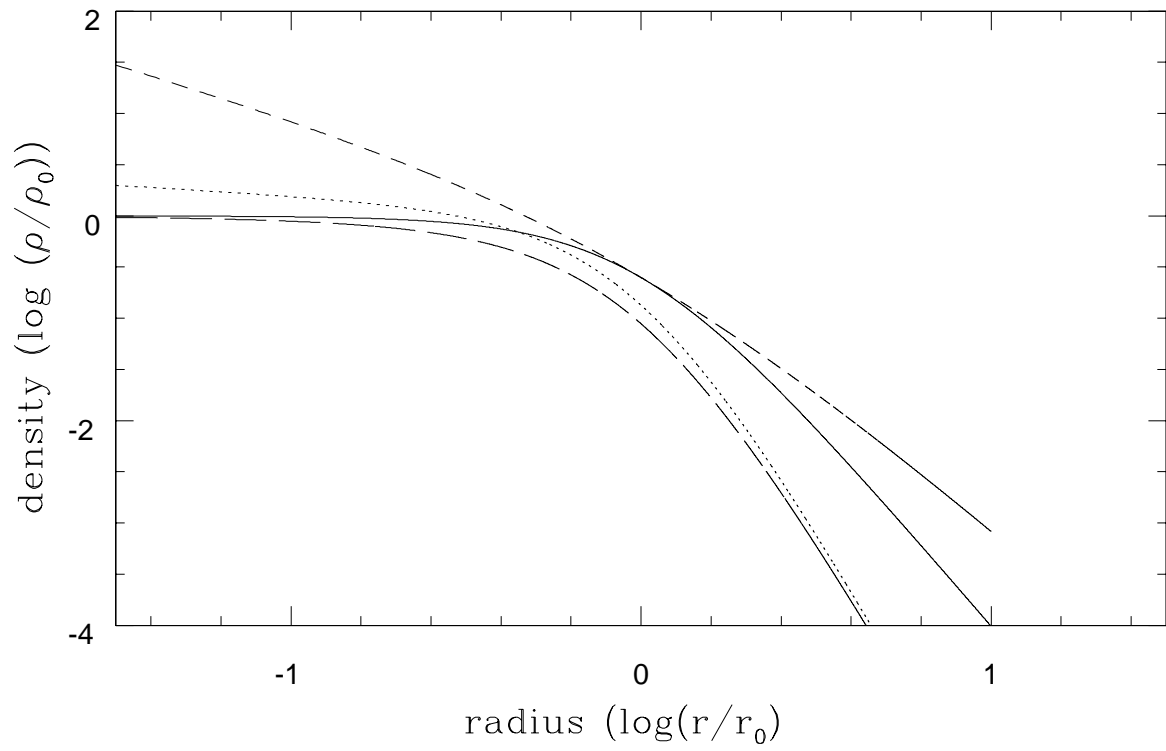


Fig. 5.— Density profiles of the four models. *solid*: pseudo-isothermal sphere, *dot*: KKBP, *long dash*: Burkert, *short dash*: NFW.

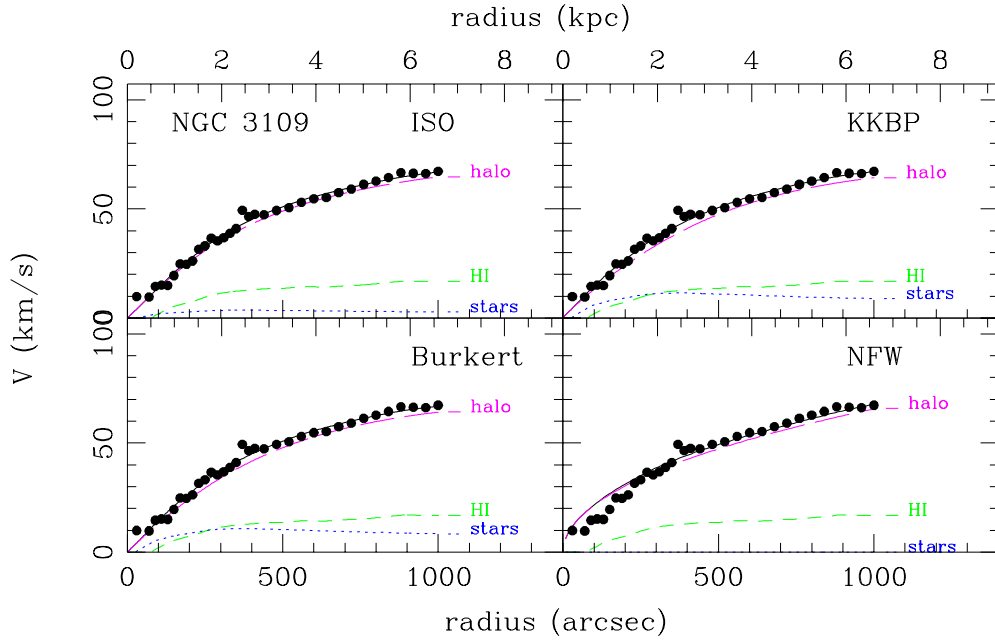


Fig. 6.— Best fit mass models for NGC 3109 using the $H\alpha$ rotation curve up to 2.7 kpc and the HI rotation curve for the rest. The dark halos density profiles are *top-left*: pseudo-isothermal sphere, *top-right*: KKBP, *bottom-left*: Burkert, *bottom-right*: NFW.

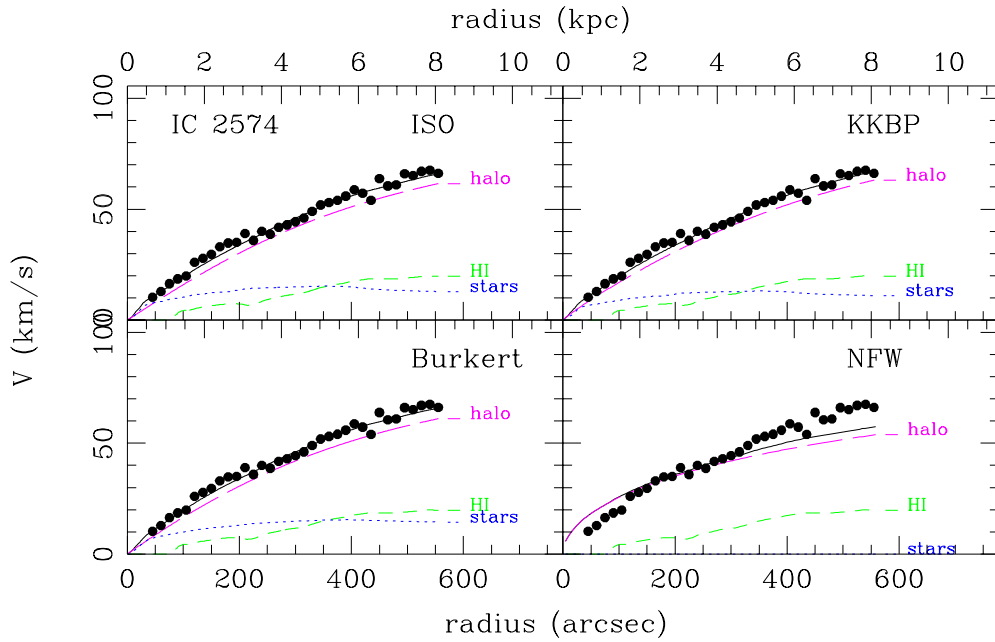


Fig. 7.— Mass models of IC 2574 using the HI rotation curve only.

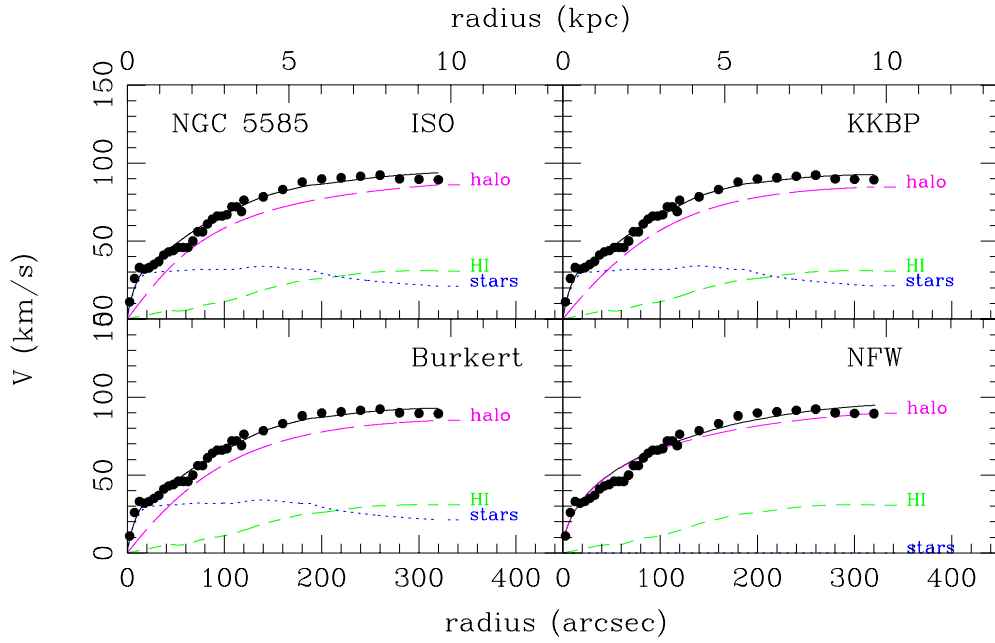


Fig. 8.— Mass models of NGC 5585 using the H α rotation curve up to 3.5 kpc and HI for the rest.

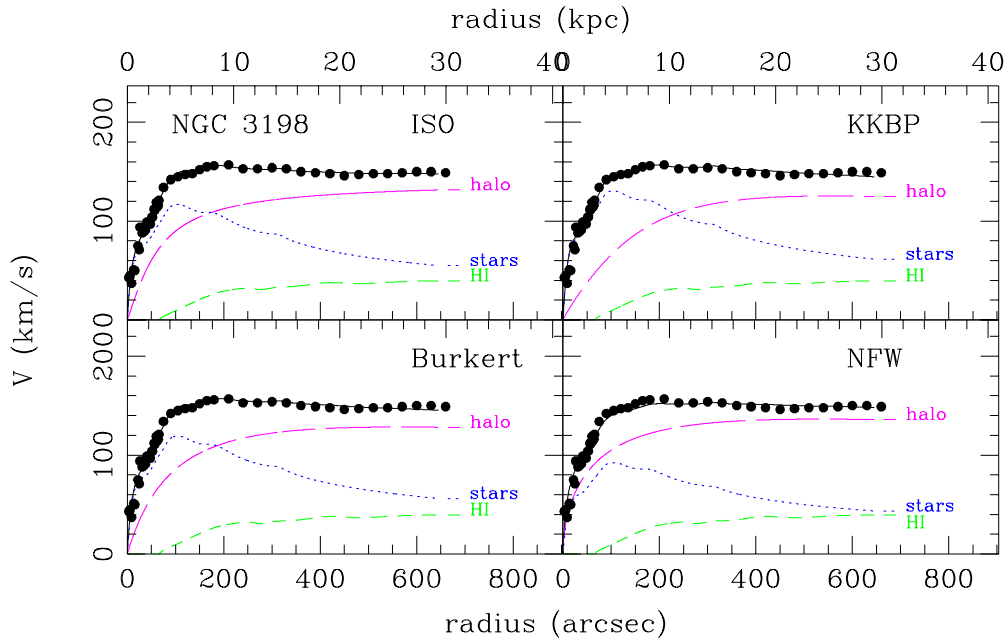


Fig. 9.— Mass models of NGC 3198 using the H α rotation curve up to 2.9 kpc and HI for the rest.

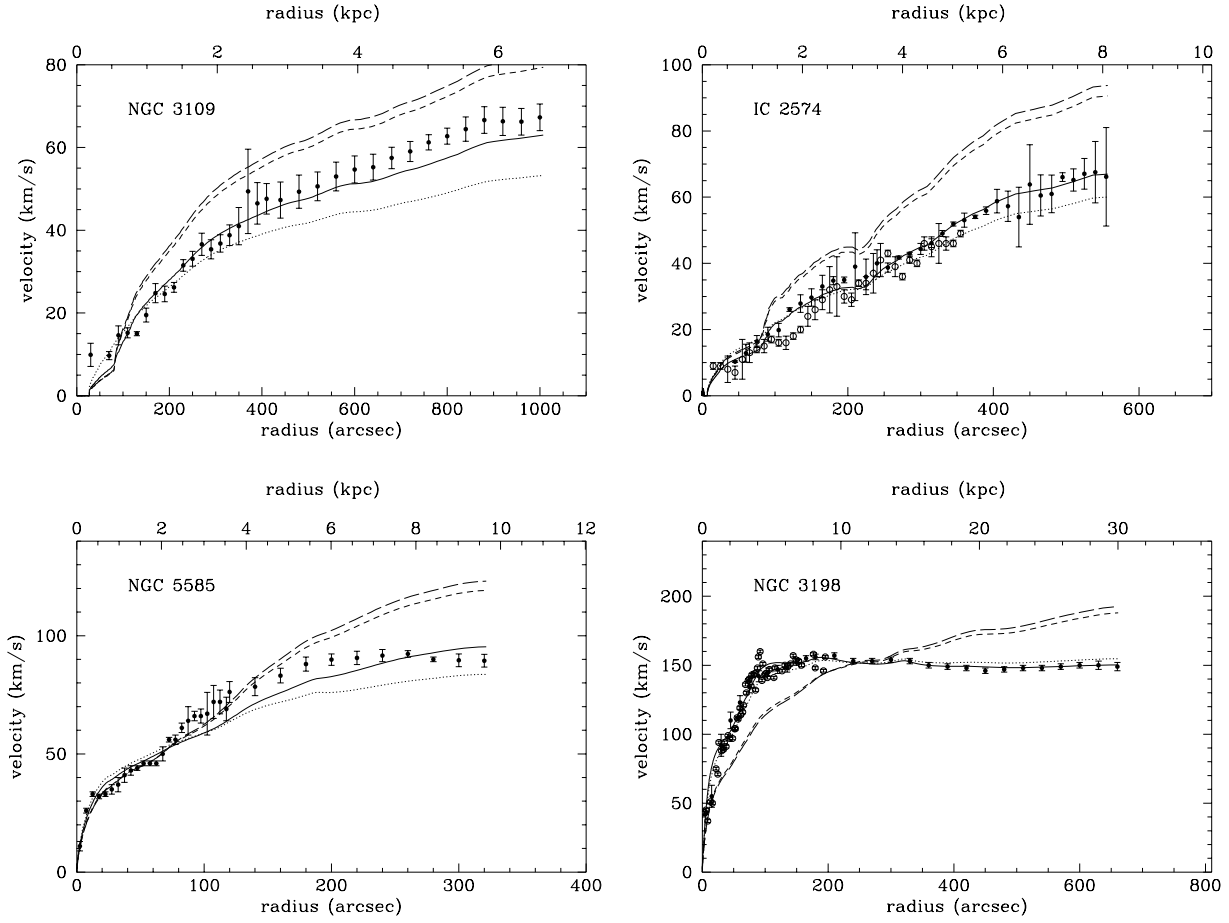


Fig. 10.— Best fit mass models using the Modified Newtonian Dynamics. Four different values of a_0 are used. Dotted line: $1.2 \times 10^{-13} \text{ km/s}^2$ (from Begeman et al. 1991), continuous line: best fit value (see Table 5), short dash: $cH_0 = 6.8 \times 10^{-13} \text{ km/s}^2$ and long dash: $c^2\sqrt{\Lambda} = 7.8 \times 10^{-13} \text{ km/s}^2$. The filled circles represent the data used in the fits (HI +H α for NGC 3109 and 5585 and HI only for IC 2574 and NGC 3198). The open circles indicates the H α velocities unused in the fits.

Table 1. Parameters of the Fabry–Perot observations.

Dates of observations	February 21 and 22, 1994
Telescope	3.6 m CFHT
Instrumentation:	
Focal plane instrument	MOSFP
CCD detector	2048×2048 Loral3, $\sigma = 8 e^{-1}$
Fabry–Perot etalon	Scanning QW1162 (CFHT1)
Interference order	1155 @ λ_{NEON}
Mean Finesse in the field	12
Calibration lamp	Neon ($\lambda = 6598.95 \text{ \AA}$)
Duration	
NGC 3109	
Per channel	7.28 min/channel
Total	3 h 24 min
Filter	$\lambda_0 = 6565.5 \text{ \AA}$, $\Delta\lambda = 12 \text{ \AA}$
IC 2574	
Per channel	8.05 min/channel
Total	3 h 45 min
Filter	$\lambda_0 = 6559.5 \text{ \AA}$, $\Delta\lambda = 12 \text{ \AA}$
Spatial Parameters:	
Field size	$8.5' \times 8.5'$
Pixel scale	$0.314'' \text{ pix}^{-1}$
Spectral Parameters:	
Number of channels	27
Free spectral range	5.66 \AA (258 km s^{-1})
Sampling	0.21 \AA (9.6 km s^{-1})/channel

Table 2. Parameters of NGC 3109.

Morphological Type ^a	SBm
RA (J2000.0)	10 ^h 03 ^m 06 ^s .6
Dec (J2000.0)	-26°09'32''
l	262 °10
b	23 °07
Adopted distance (Mpc) ^b	1.36
	(1' \simeq 0.396 kpc)
Mean axis ratio, $q = b/a^c$	0.28 \pm 0.02
Inclination, i^c	75 ° \pm 2 °
Isophotal major diameter, D_{25}^c	14.4 '
Major axis PA ^c	93 ° \pm 2°
Exponential scale length (kpc) ^c	1.2
Holmberg radius, R_{HO}^c	13.3 '
Absolute magnitude, M_B^c	-16.35
Total luminosity, L_B	$5.19 \times 10^8 L_{\odot}$
Helio. radial velocity (km s ⁻¹) ^c	404 \pm 3

^aDe Vaucouleurs et al. (1991)

^bMusella et al. (1997)

^cJobin & Carignan (1990)

Table 3. Optical parameters of IC 2574.

Morphological Type ^a	SABm
RA (J2000.0)	10 ^h 28 ^m 21 ^s .2
Dec (J2000.0)	68°24′43″
l	140 °21
b	43 °60
Adopted distance (Mpc) ^b	3.0
	(1′ \simeq 0.8 kpc)
Mean axis ratio, $q = b/a$ ^b	0.48 \pm 0.06
Inclination, i ^b	75 ° \pm 3 °
Isophotal major diameter, D_{25} ^b	9.76 ′
Major axis PA ^b	52 ° \pm 6°
Exponential scale length (kpc) ^b	2.2
Holmberg radius, R_{HO} ^b	8.63 ′
Absolute magnitude, M_B ^b	−16.77
Total luminosity, L_B	$7.94 \times 10^8 L_{\odot}$
Helio. radial velocity (km s ^{−1}) ^b	58 \pm 3

^aDe Vaucouleurs et al. (1991)

^bMartimbeau et al. (1994)

Table 4. Parameters of the mass models.

Model	Galaxy	Type	$(\mathcal{M}/L_B)_*$	r_0 kpc	ρ_0 $10^{-3} \mathcal{M}_\odot / \text{pc}^{-3}$	χ^2
ISO	IC 2574	SABm	0.34	5.4	7.0	2.7
	NGC 3109	SBm	0.04	2.35	2.50	2.8
	NGC 5585	SABd	0.85	2.15	4.25	4.4
	NGC 3198	SBc	4.80	2.54	5.70	7.1
Burkert	IC 2574	SABm	0.6	8.0	8.4	2.5
	NGC 3109		0.35	4.1	2.50	2.9
	NGC 5585		0.086	4.0	4.0	8.21
	NGC 3198		5.0	5.8	7.40	7.70
KKBP	IC 2574	SABm	0.25	9.2	5.0	2.43
	NGC 3109		0.4	4.5	1.45	2.9
	NGC 5585		0.86	3.9	5.6	7.4
	NGC 3198		6.0	9.15	1.14	9.1
NFW	IC 2574	SABm	0.0	35	0.05	44.0
	NGC 3109		0.00	109	0.024	10.18
	NGC 5585		0.00	10.1	0.77	7.86
	NGC 3198		3.0	11.20	1.27	44.4

Note. — In terms of the concentration parameter c , $\rho_0 = \frac{200}{3} \frac{c^3}{\ln(1+c)-c/(1+c)}$

Table 5. MOND parameters when using the best fitted a_0 .

Galaxy	Distance Mpc	a_0 $\times 10^{-13} \text{ km/s}^2$	$(\mathcal{M}/L_B)_*$	χ^2 $\mathcal{M}_\odot/L_\odot$
IC 2574	3.0	2.0	0.02	1.51
NGC 3109	1.36	2.68	0.12	4.99
NGC 5585	6.2	2.45	0.34	5.94
NGC 3198	9.36	0.9	6.71	1.11

Table 6. Optical rotation curve of NGC 3109 at $20''$ binning from ROCUR. The two sides and the global rotational velocities are computed independently. The later are corrected for asymmetric drift.

R_{sides} "	V_{app} km s^{-1}	V_{rec} km s^{-1}	R "	V km s^{-1}
35	8 ± 1	3 ± 1	30	10 ± 2
65	6 ± 1		70	10 ± 1
95	15 ± 1		90	15 ± 1
			110	15 ± 1
125	14 ± 1		130	15 ± 1
155	22 ± 2		150	20 ± 1
			170	25 ± 1
185	25 ± 1		190	25 ± 1
215	26 ± 1		210	26 ± 1
			230	32 ± 1
245	32 ± 1		250	33 ± 1
275	34 ± 1	33 ± 1	270	37 ± 2
			290	35 ± 2
305	35 ± 1	32 ± 135	310	37 ± 2
335	39 ± 2	37 ± 1	330	39 ± 2
			350	41 ± 4
365	46 ± 6	40 ± 8	370	49 ± 10
395	52 ± 9	42 ± 4	390	47 ± 2
			410	48 ± 1
425	46 ± 2	45 ± 11		

Note. — derived with $V_s = 402 \text{ km s}^{-1}$

Table 7. Optical rotation curve of IC 2574 at $9.4''$ binning from ADHOC. The two sides are computed independently and the total is their mean average by the number of points. The velocity dispersion and the number of points appear for both sides while the error is the two σ/N added in quadrature.

R arcsec	N_{app}	V_{app} km s^{-1}	σ_{ring} km s^{-1}	N_{rec}	V_{rec} km s^{-1}	σ_{ring} km s^{-1}	V km s^{-1}
8				2	22	8	22 ± 5
12				3	34	9	34 ± 5
15	22	8	20				8 ± 4
24	36	15	10	79	10	7	11 ± 1
33	26	12	12	81	3	27	5 ± 3
43	22	2	10				2 ± 2
52	62	10	15	144	3	22	5 ± 2
61	101	17	22	206	6	17	10 ± 2
70	139	27	24	228	9	16	16 ± 1
80	151	30	29	200	14	14	21 ± 2
89	113	42	37	202	16	16	25 ± 2
99	62	43	23	174	29	13	33 ± 2
108	75	33	23	157	30	16	31 ± 2
118	78	31	25	144	32	20	32 ± 2
127	72	33	27	137	31	19	32 ± 2
137	53	53	28	206	25	12	30 ± 2
146	40	66	26	423	26	9	30 ± 1
155	41	79	33	646	28	8	31 ± 1
165	45	54	40	739	31	13	32 ± 2
174	68	37	46	734	32	11	33 ± 2
183	81	25	18	712	34	10	33 ± 1
193	94	30	15	593	36	6	35 ± 1
202	102	31	22	510	36	8	35 ± 1
212	141	32	29	457	37	12	36 ± 1
221	193	34	24	410	40	13	38 ± 1
230	155	30	22	309	44	16	40 ± 1
240	147	42	34	418	48	12	47 ± 2
249	139	42	34	487	48	14	46 ± 1
259	185	43	28	497	46	15	45 ± 1
268	190	40	21	372	43	12	42 ± 1
278	138	44	23	234	40	21	41 ± 2
287	245	39	20	262	34	19	36 ± 1
296	287	44	13	258	34	28	39 ± 1
306	289	42	10	279	45	24	44 ± 1
314	279	38	11	218	42	23	40 ± 1
325	188	36	20	172	40	24	38 ± 2
334	347	37	20	195	45	31	40 ± 2

Table 7—Continued

R arcsec	N_{app}	V_{app} km s^{-1}	σ_{ring} km s^{-1}	N_{rec}	V_{rec} km s^{-1}	σ_{ring} km s^{-1}	V km s^{-1}
343	258	36	20	177	45	29	40 ± 2
352	159	40	13	183	47	27	44 ± 2
362	182	42	8	181	44	24	43 ± 1
372	327	44	15	175	46	23	45 ± 1
381	440	43	12	205	47	25	45 ± 1
390	255	40	18	217	53	28	46 ± 2
400	225	39	20	223	49	25	44 ± 2
409	162	41	29	291	52	26	48 ± 2
418	174	47	20	360	57	29	54 ± 1
428	162	50	42	424	60	32	57 ± 2
437	159	52	33	446	58	36	57 ± 2
446	171	46	31	367	55	27	52 ± 2
456	167	52	25	317	45	24	48 ± 2
466	173	55	23	343	48	28	51 ± 2
475	224	55	29	332	52	30	53 ± 2
484	240	59	45	339	54	28	56 ± 2
494	214	60	28	363	59	28	59 ± 2
503	171	64	36	434	60	22	61 ± 2
512	126	77	33	437	58	31	62 ± 2
522	96	70	15	504	59	37	61 ± 2
531	87	63	12	519	63	36	63 ± 2
540	85	73	32	511	62	37	64 ± 2
550	90	81	45	537	64	41	66 ± 2
559	65	71	30	505	65	39	66 ± 2
568	36	77	17	549	68	36	68 ± 2
578	17	85	25	553	64	35	65 ± 2
587	18	81	4	517	63	35	64 ± 2
595	3	79	4	433	55	42	55 ± 2
606				465	60	38	60 ± 2
616				496	67	36	67 ± 2
625				521	76	37	76 ± 2
634				531	79	35	79 ± 2
645	8	60	78	518	82	36	82 ± 4
653	19	101	75	513	82	41	82 ± 4
663				478	71	43	71 ± 2
672				476	70	36	70 ± 2
682				462	69	42	69 ± 2

Table 7—Continued

R arcsec	N_{app}	V_{app} km s^{-1}	σ_{ring} km s^{-1}	N_{rec}	V_{rec} km s^{-1}	σ_{ring} km s^{-1}	V km s^{-1}
691				465	78	38	78 ± 2
700				465	88	38	88 ± 2
710				460	87	39	87 ± 2
719				421	83	31	83 ± 1
728				348	85	29	85 ± 2
738				342	94	20	94 ± 1
747				323	94	20	94 ± 1
757				282	95	24	95 ± 1
766				280	93	25	93 ± 2
776				255	92	34	92 ± 2
785				268	97	33	97 ± 2
794				277	97	40	97 ± 2
803				215	99	46	99 ± 3
813				163	101	42	101 ± 3
823				115	110	32	110 ± 3
869				61	120	14	119 ± 2
877				24	103	12	102 ± 2

Note. — derived with $V_s = 53 \text{ km s}^{-1}$, $i = 75^\circ$, $\text{PA} = 52^\circ$